Journal of the Society for Cardiovascular Angiography & Interventions 2 (2023) 100570

JSCAI

The official journal of the Society for Cardiovascular Angiography & Interventions

Original Research

Radial Wall Strain Assessment From AI-Assisted Angiography: Feasibility and Agreement With OCT as Reference Standard

Jiayue Huang, MSc [a], Shengxian Tu, PhD [b,*], Chunming Li, BSc [b], Huihong Hong, MD [c], Zhiqing Wang, MD [c], Lianglong Chen, MD, PhD [c], Juan Luis Gutiérrez-Chico, MD, PhD [d], William Wijns, MD, PhD [a]

[a] *The Lambe Institute for Translational Medicine, Smart Sensors Laboratory and Curam, University of Galway, Galway, Ireland;* [b] *Biomedical Instrument Institute, School of Biomedical Engineering, Shanghai Jiao Tong University, Shanghai, China;* [c] *Department of Cardiology, Fujian Medical University Union Hospital, Fuzhou, China;* [d] *Bundeswehrzentralkrankenhaus (Federal Army Central Military Hospital), Koblenz, Germany*

ABSTRACT

Background: High-strain spots in coronary arteries are associated with plaque vulnerability and predict future events. Artificial intelligence currently enables the calculation of radial wall strain (RWS) from coronary angiography (RWS_{Angio}). This study aimed to determine the agreement between novel RWS_{Angio} and RWS derived from optical coherence tomography (OCT) followed by finite element analysis, as the established reference standard (RWS_{OCT}).

Methods: All lesions from a previous OCT study were enrolled. OCT was automatically coregistered with angiography. RWS_{Angio} was computed as the relative luminal deformation throughout the cardiac cycle, whereas RWS_{OCT} was analyzed using finite element analysis on OCT cross-sections at 1-mm intervals. The luminal deformation in the direction of minimal lumen diameter was used to derive RWS_{OCT}, using the same definition as RWS_{Angio}. The maximal RWS_{OCT} and RWS_{Angio} at healthy segments adjacent to the interrogated lesion were also analyzed.

Results: Finite element analysis was performed in 578 OCT cross-sections from 45 lesions stemming from 36 patients. RWS_{Angio} showed good correlation and agreement with RWS_{OCT} ($r = 0.91$; $P < .001$; Lin coefficient = 0.85). RWS_{Angio} in atherosclerotic segments was significantly higher than that in healthy segments (12.6% [11.0, 16.0] vs 4.5% [2.9, 5.5], $P < .001$). The intraclass correlation coefficients for intra- and interobserver variability in repeated RWS_{Angio} analysis were 0.92 (95% CI, 0.87-0.95) and 0.88 (95% CI, 0.81-0.92), respectively. The mean analysis time of RWS_{OCT} and RWS_{Angio} for each lesion was 95.0 ± 41.1 and 0.9 ± 0.1 minutes, respectively.

Conclusions: Radial wall strain from coronary angiography can be rapidly and easily computed solely from angiography, showing excellent agreement with strain derived from coregistered OCT. This novel and simple method might provide a cost-effective biomechanical assessment in large populations.

Introduction

The rupture and subsequent thrombosis of a vulnerable plaque is recognized as the main pathologic substrate for acute coronary syndrome.[1,2] Nonetheless, clinical translation of the concept of plaque vulnerability is still a matter of dispute[3] because morphological features of vulnerability, including thin-cap fibroatheroma or plaque burden as detected by optical coherence tomography (OCT) or intravascular ultrasound (IVUS), have shown low specificity for prospectively predicting future adverse events in individual patients.[4–9]

The direct biomechanical assessment of plaque represents an appealing alternative to its purely morphological characterization to estimate vulnerability, although it has been restricted to few selected patients so far because of methodological limitations. From a biomechanical point of view, fatigue and rupture of a fibrous cap are caused by repetitive high circumferential stress, which translates into increased radial strain, both as a result of the pulsatile rise and fall of intracoronary pressure and its interaction with plaque composition.[10–15] In addition, high-strain spots were found to correlate with OCT-derived features of vulnerability.[16] Therefore, the identification of high-strain spots within the stenotic segment might potentially improve the risk assessment.[10–15] Coronary strain can either be measured using intravascular elastography and palpography[12–14,17–20] or computed by means of finite element analysis (FEA).[21] However, the requirement for dedicated

Abbreviations: DS, diameter stenosis; FEA, finite element analysis; FFR, fractional flow reserve; IVUS, intravascular ultrasound; LDC, lumen diameter change; LSR, lumen symmetry ratio; MLD, minimal lumen diameter; OCT, optical coherence tomography; RWS, radial wall strain.

Keywords: coronary angiography; coronary strain; finite element analysis; optical coherence tomography.

* Corresponding author: sxtu@sjtu.edu.cn (S. Tu).

https://doi.org/10.1016/j.jscai.2022.100570
Received 12 September 2022; Received in revised form 30 November 2022; Accepted 2 December 2022;
Available online 23 December 2022

and costly intracoronary imaging devices, together with the laborious and time-consuming analytical procedures, have prevented the clinical application of this promising biomechanical concept on a large scale.

As one of the most important components of coronary strain, the radial wall strain (RWS) directly reflects the interplay between cyclic pulsatile intravascular pressure and tissue composition of the vessel wall.[22,23] A previous OCT FEA study has demonstrated good concordance between cyclic luminal deformation and high-strain spots within the lesion, thus setting the preamble for a simplified biomechanical assessment using dynamic angiography.[21] Empowered by artificial intelligence (AI), a novel method was proposed to calculate RWS from a single angiographic projection (RWS_{Angio}) and has been validated against coregistered OCT images. RWS_{Angio} correlated well with lesion morphology and showed good performance in identifying the presence of vulnerable plaques.[16] The current study aimed to report its agreement with the RWS derived from coregistered OCT images after FEA calculation.

Methods

Study design and population

All de novo lesions identified with a diameter stenosis (DS) of 40% to 90% by visual estimation, from a previous OCT FEA study and coregistered with intracoronary pressure recordings, were analyzed.[21] Details about the inclusion and exclusion criteria, image acquisition, and intracoronary pressure measurement are described in the Supplemental File.

The institutional review board approved the post hoc analysis of the data. The study complied with the principles of good clinical practice and with the Declaration of Helsinki for investigations in humans. The local Ethics Committee of Campo de Gibraltar Health Trust approved the protocol, and each patient gave written informed consent before inclusion.

OCT and angiography coregistration

Details about the automated coregistration between OCT and angiogram (Figure 1A, B, C, and Figure 2A, B, C) are described in the Supplemental File. The OCT cross-section with minimal lumen area was used to derive the lumen symmetry ratio (LSR), calculated as the minimal lumen diameter (MLD) divided by the maximal lumen diameter. Lesions with an LSR of <0.7 were defined as asymmetric.[24] The MLD derived from both modalities was also recorded.

RWS_{Angio} and RWS_{OCT} analysis

Radial wall strain derived from angiography (RWS_{Angio}) and from OCT (RWS_{OCT}) were analyzed by 2 analysts (H.H. and J.H.) who were blinded to each other's results. RWS_{Angio} analysis was performed using a commercially available software package (AngioPlus Core, Version 3, Pulse Medical). The standard operation procedure for RWS_{Angio} analysis has been previously described.[16] Briefly, the angiographic projections with minimal lesion overlap and foreshortening were manually selected and imported into the software to compute the dynamic changes of luminal deformation over the cardiac cycle, which were determined by a combination of cyclic intravascular pressure change and the tissue compositions inside the vessel wall.[22,23] The lesion with the most severe stenosis was automatically detected for RWS_{Angio} analysis. Aided by AI, 4 frames with sharp lumen contours at representative cardiac phases, ie, end-diastole, early-systole, end-systole, and mid-diastole, were automatically selected, followed by automated lumen contour delineation (Figures 1D1-D4 and 2D1-D4). The lumen diameters at the 4 cardiac phases were automatically matched by the software. In case of suboptimal frame selection, lumen delineation, lesion selection, or inappropriate matching of the cardiac phases, manual edition was allowed. The lumen diameter change (LDC) at every longitudinal position along the interrogated lesion was then computed as the maximal diameter over the cardiac cycle minus the minimal diameter over the cardiac cycle. The RWS_{Angio} was then calculated as the angiography-derived LDC (LDC_{Angio}) divided by the maximal diameter.

Radial wall strain derived from OCT was calculated by means of FEA using cross-sections at 1-mm intervals within each coregistered lesion. OCT cross-sections were excluded from FEA when the vessel structure was not completely imaged, insufficient blood clearance precluded the visualization of plaque components and vessels, and side branches were present within the intima. The methodology for OCT-based FEA analysis has been previously reported.[21] Briefly, the tissue encompassed between the lumen and internal elastic lamina contours was automatically analyzed and characterized using AI.[25] Based on the OCT tissue characterization, the geometric models for FEA were reconstructed taking into account 5 essential mechanically relevant components (lipids, calcium, fibrous tissue, media, and adventitia). The FEA model of each analyzed OCT cross-section was loaded with the position-specific intracoronary pressure, which was derived from the intracoronary tracing data recorded at the distal position by the pressure wire, in combination with the computed optical flow ratio pullback curve to determine the pressure at each cross-section (Figures 1E and 2E).[21] After FEA, the luminal deformation during the whole cardiac cycle could be obtained. The maximal luminal deformation in the axis defined by the MLD was used to calculate the OCT-derived lumen diameter change (LDC_{OCT}) and subsequently the OCT-derived radial wall strain (RWS_{OCT}) (Figures 1G and 2G), following the same definition as LDC_{Angio} and RWS_{Angio}, respectively (Central Illustration, Figures 1B7 and 2B4).

For each interrogated lesion, RWS_{Angio} and RWS_{OCT} analyses were also performed on the normal segments adjacent to the lesions. These unobstructed normal segments were carefully selected based on coregistered OCT images and defined as the segment where neither atherosclerotic plaque nor side branches were observed on OCT for at least 5 mm. For both RWS_{Angio} and RWS_{OCT}, the maximal RWS values in each interrogated lesion and normal segment were recorded as lesion RWS and normal RWS, respectively.

Reproducibility of RWS_{Angio} analysis

All interrogated lesions were reanalyzed by the same analyst 3 months later and by a second analyst using the same standard operation procedures; the analysts were blinded to each other's or to the previous computational results.

Statistical analysis

Descriptive statistics for continuous variables were presented as mean $\pm$ standard deviation if the data followed a Gaussian distribution or as median (quartiles) if a Gaussian distribution could not be assumed. Categorical variables are reported as numbers (percentages). Correlations were evaluated using the Spearman coefficient. Differences between groups in continuous variables were assessed using Mann-Whitney test for unpaired comparisons, whereas the Wilcoxon signed-rank test was used for pairwise comparisons. To estimate constant or proportional biases between OCT-derived and angiography-derived results, the Passing-Bablok nonparametric regression analysis was performed using OCT-derived values along the y-axis. The Lin coefficient was used to test the agreement between different continuous variables. All statistical analyses were performed using SPSS version 27.0 (IBM Corp.). A 2-sided value of P value of $<.05$ was considered statistically significant.

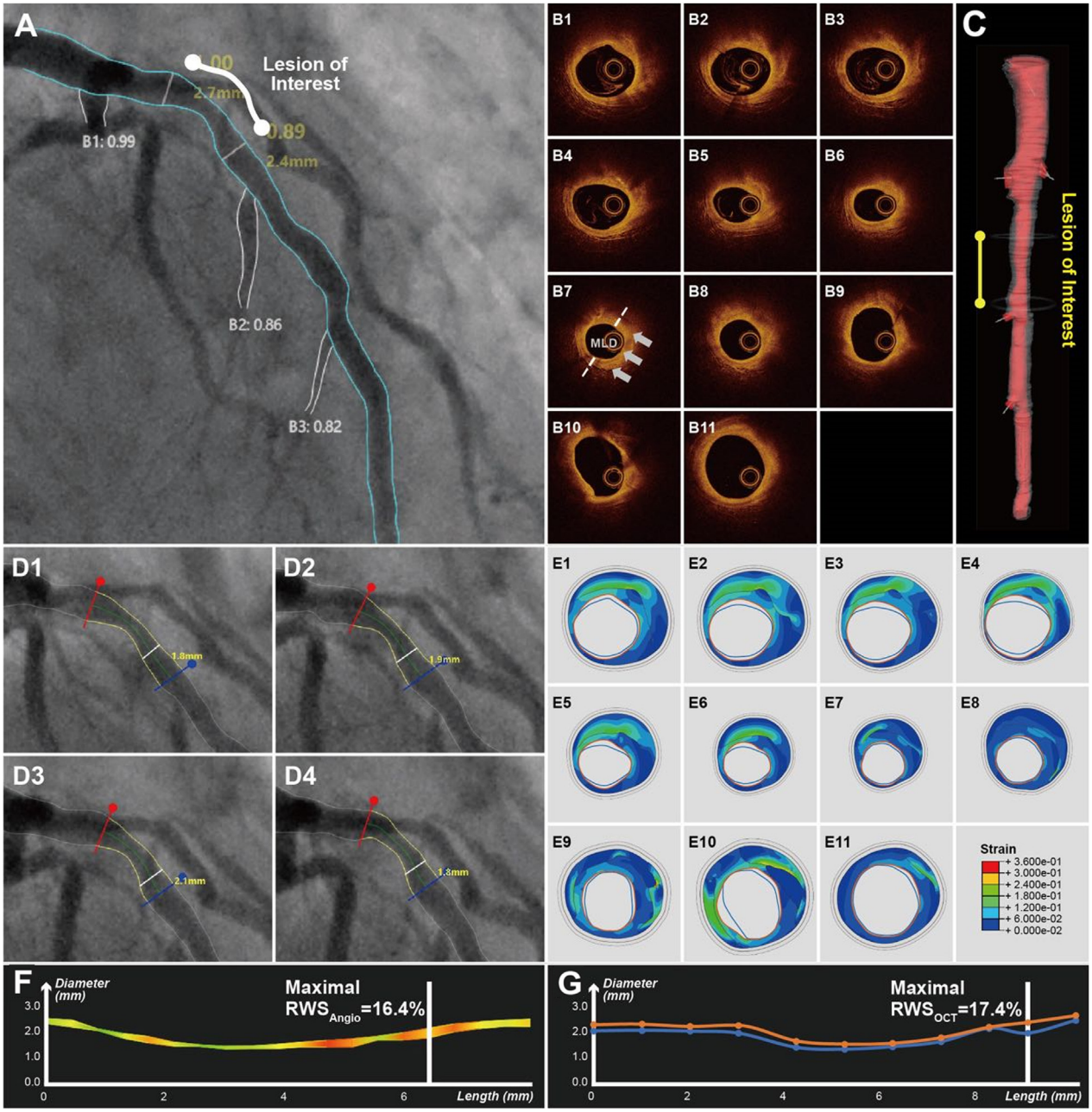

Figure 1.

A representative case showing an intermediate left anterior descending artery (LAD) lesion with high radial wall strain from coronary angiography (RWS_{Angio}) and radial wall strain derived from optical coherence tomography (RWS_{OCT}). An intermediate LAD lesion was observed in coregistered angiography (**A**) and optical coherence tomography (OCT) images (**B and C**). Finite element analysis was performed on OCT cross-sections at 1-mm intervals (**B1-B11**). The luminal deformation in the direction of minimal lumen diameter was used to derive RWS_{OCT} for each cross-section (**B7**). In angiography, 4 representative moments (ie, end-systole, mid-diastole, end-diastole, and early-systole) were selected to compute RWS_{Angio} (**D1-D4**). (**E1-E11**) OCT-derived strain distribution. As a result, the lesion RWS_{Angio} and RWS_{OCT} were 16.4% and 17.4%, respectively (**F and G**).

Results

Baseline clinical and lesion characteristics

Finite element analysis was performed in 578 OCT cross-sections from 45 lesions from 37 vessels stemming from 36 patients. Five lesions were excluded because of vessel overlap (n = 3) or small vessel diameter (n = 2) (Figure 3). The baseline demographic and lesion characteristics are presented in Tables 1 and 2, respectively. The mean vessel fractional flow reserve (FFR) was 0.83 ± 0.08, and the median pressure drop across the lesion was 0.05 [0.03, 0.08], as computed from the optical flow ratio pullback curve. The median %DS was 35% [31, 40] by quantitative angiography. The lesion length derived from OCT was slightly longer than the one derived from angiography (11.6 ± 3.4 mm versus 10.4 ± 3.3 mm; $P < .001$). The MLD derived from angiography was larger than the one derived from OCT (1.80 mm [1.57, 2.00] versus 1.59 mm [1.46, 1.79], $P < .001$).

Agreement between RWS_{Angio} and RWS_{OCT}

A total of 45 lesion RWS and 25 normal RWS were included for paired comparison. The average LDC_{Angio} and RWS_{Angio} were 0.24 mm [0.15, 0.33] and 10.6% [5.3, 14.5], respectively. The OCT-derived results

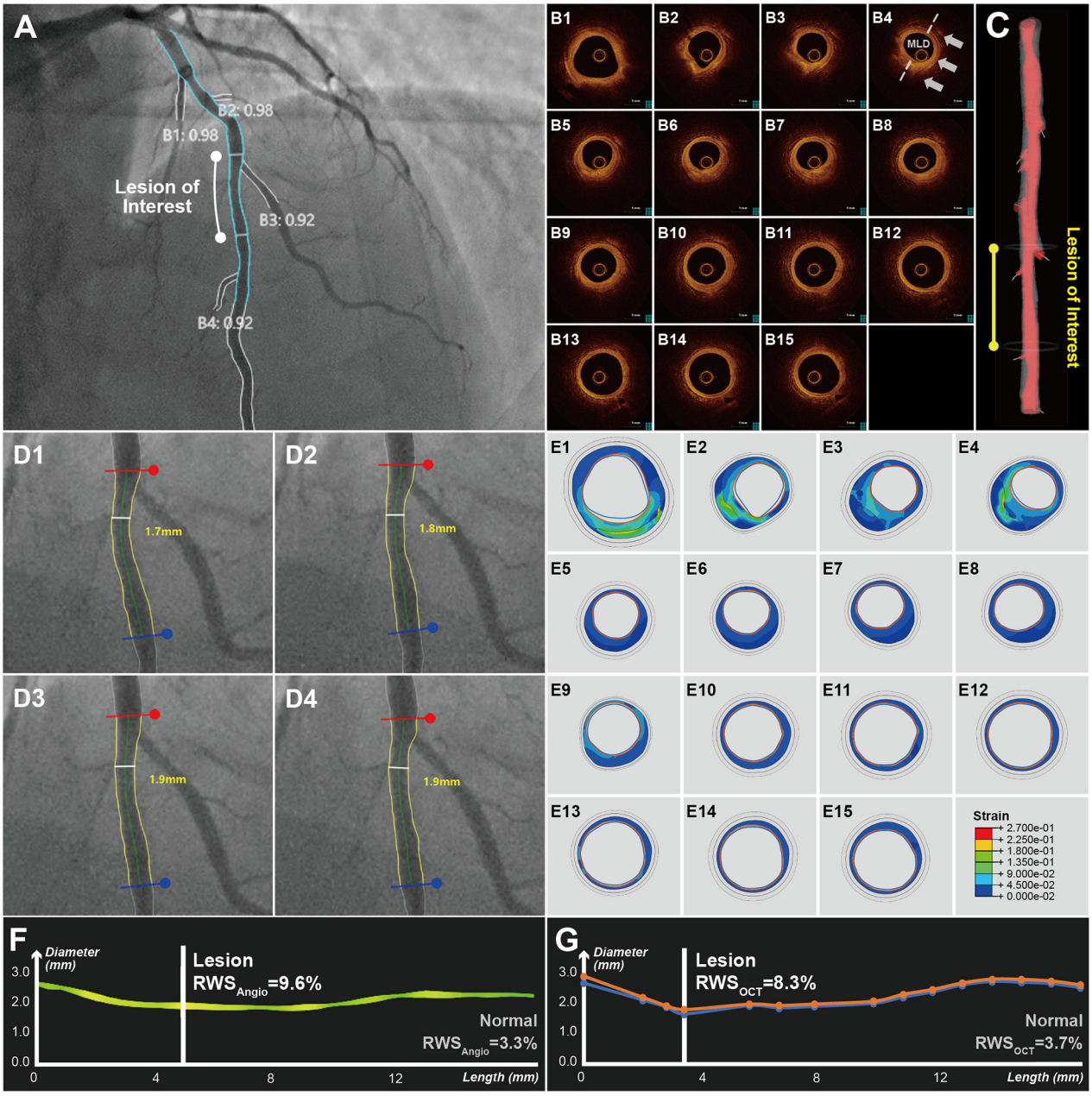

Figure 2.

A representative case showing an intermediate left anterior descending artery (LAD) lesion with low radial wall strain from coronary angiography (RWS_{Angio}) and radial wall strain derived from optical coherence tomography (RWS_{OCT}). An intermediate LAD lesion was observed on coregistered angiography (**A**) and optical coherence tomography (OCT) images (**B and C**). Finite element analysis was performed on OCT cross-sections at 1-mm intervals (**B1-B15**). The luminal deformation in the direction of minimal lumen diameter was used to derive RWS_{OCT} for each cross-section (**B4**). In angiography, 4 representative moments (ie, end-systole, mid-diastole, end-diastole, and early-systole) were selected to compute RWS_{Angio} (**D1-D4**). **E1-E15** show OCT-derived strain distribution. As a result, the lesion RWS_{Angio} and RWS_{OCT} were 9.6% and 8.3%, respectively. The distal normal RWS_{Angio} and RWS_{OCT} were 3.3% and 3.7%, respectively (**F and G**).

were not significantly different from angiography, being 0.24 mm [0.13, 0.36] ($P = .340$) for LDC_{OCT} and 8.1% [4.7, 15.6] for RWS_{OCT} ($P = .449$). The numerical concordance between RWS_{Angio} and RWS_{OCT} remained between subgroups with %DS of ≥35% and with %DS of <35% (RWS_{Angio} - RWS_{OCT} = 0.6% versus 0.5%, $P = .802$). The locations of maximal RWS_{Angio} and maximal RWS_{OCT} within each analyzed lesion were exactly matched in 31.1% of the cases. The distance between the 2 maximal RWS locations was within half of the lesion length in 86.7% of the cases.

Passing-Bablok nonparametric regression and Bland-Altman plots for LDC and RWS derived from both modalities are presented in Figure 4. Good correlation and agreement were observed between LDC_{OCT} and LDC_{Angio} ($r = 0.86$; $P < .001$; Lin coefficient = 0.82), and between RWS_{OCT} and RWS_{Angio} ($r = 0.91$; $P < .001$; Lin coefficient = 0.85). RWS_{Angio} incurred a constant and proportional bias with respect to RWS_{OCT}, with the slope being 1.21 and the intercept being −2.18%.

Using the median lesion RWS_{Angio} and median lesion RWS_{OCT} as the cut-off values to identify biomechanically abnormal lesions with high strain, RWS_{Angio} showed substantial agreement with RWS_{OCT} (kappa = 0.78, with 19 true positive, 21 true negative, 3 false negative, and 2 false positive) and excellent diagnostic performance (area under the curve = 0.96).

Lesion RWS_{Angio} in non–flow-limiting vessels were not significantly different from flow-limiting vessels with FFR of ≤0.80 (13.1% [11.0, 15.8]

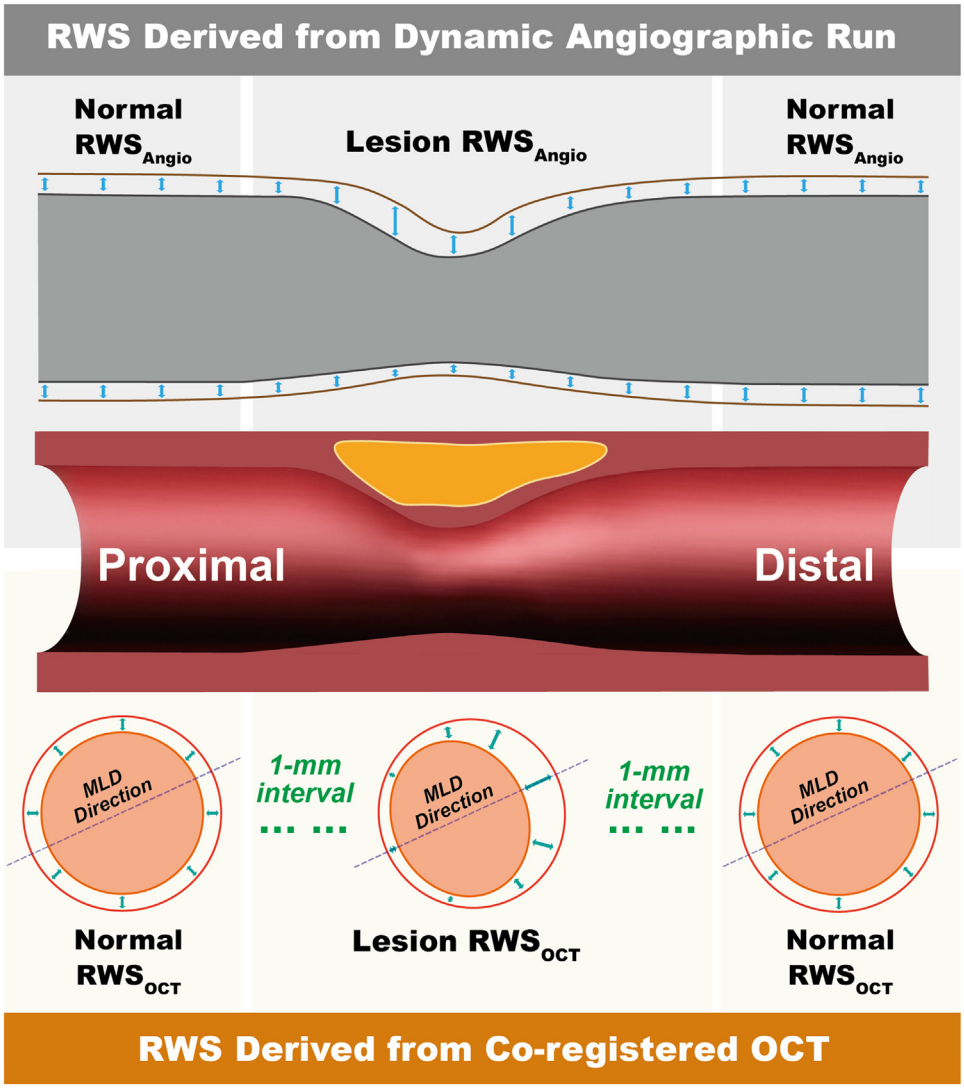

Central Illustration.
Validation for angiography-derived radial wall strain (RWS) using optical coherence tomography (OCT)–derived strain. For each interrogated lesion, angiography and OCT were automatically coregistered. RWS_{Angio} was computed at every longitudinal position of the analyzed segment, whereas RWS_{OCT} was analyzed on OCT cross-sections at 1-mm intervals and computed in the direction of minimal lumen diameter (MLD). For both angiography and OCT, the maximal RWS value along the stenotic segment was recorded as lesion RWS, whereas the maximal RWS value in healthy segments, as confirmed in coregistered OCT images, adjacent to the lesion, was recorded as normal RWS.

for the FFR of >0.80 group versus 12.6% [10.9, 16.6] for the FFR of ≤0.80 group; $P = .953$). The same applied to RWS_{OCT} (FFR of >0.80 group versus FFR of ≤0.80 group: 12.8% [8.5, 18.2] versus 13.1% [8.2, 17.5]; $P = .888$).

Lesion RWS versus normal RWS

Table 3 shows the LDC and RWS at stenotic and normal segments. The lesion LDC_{Angio} was not significantly different from LDC_{OCT} (LDC_{Angio} versus LDC_{OCT}: 0.29 mm [0.24, 0.38] versus 0.29 mm [0.19, 0.46], $P = .765$). The same applied to the computation of RWS (RWS_{Angio} % versus RWS_{OCT}: 12.6% [11.0, 16.0] versus 13.1% [8.2, 17.7], $P = .800$).

The lesion RWS_{Angio} was significantly larger than normal RWS_{Angio} (12.6% [11.0, 16.0] versus 4.5% [2.9, 5.5]; $P < .001$). The same applied to FEA results from coregistered OCT (lesion $RWS_{OCT} = 13.1\%$ [8.2, 17.7] versus normal $RWS_{OCT} = 3.7\%$ [2.4, 5.5]; $P < .001$).

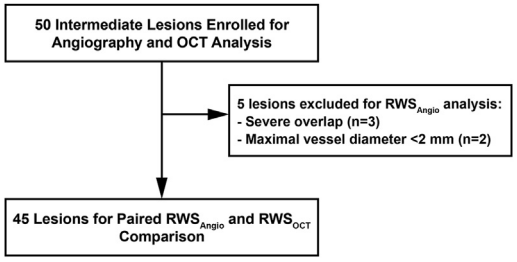

Figure 3.
Study flow chart. OCT, optical coherence tomography; RWS, radial wall strain.

Impact of plaque morphology

The mean lipidic plaque volume and calcified plaque volume within each lesion were 15.1 mm^3 [8.3, 26.0] and 4.6 mm^3 [0.3, 4.6]. A larger numerical discrepancy between MLD derived from OCT and angiography was observed for asymmetric lesions than for symmetric lesions (0.44 mm [0.21, 0.51] versus 0.05 mm [−0.01, 0.21], $P = .001$).

The differences between RWS_{OCT} and RWS_{Angio} were negatively correlated with LSR ($r = -0.55$, $P < .001$). A total of 11 of 13 (85%) asymmetric lesions showed high strain by both indices (agreement between RWS_{Angio} and $RWS_{OCT} = 100\%$), whereas for symmetric lesions, 34% and 41% high-strain lesions were identified by RWS_{OCT} and RWS_{Angio}, respectively, leading to an agreement of 81%.

Table 1. Baseline demographic characteristics.

	Patients (N = 36)
Age, y	63 ± 11
Women	3/36 (8.3%)
BMI, kg/m^2	28.4 [25.4, 30.1]
Diabetes mellitus	12/36 (33.3%)
Hypertension	24/36 (66.7%)
Hyperlipidemia	16/36 (44.4%)
Current smoker	12/36 (33.3%)
Family history of CAD	2/36 (5.5%)
Previous PCI	28/36 (77.8%)
Previous CABG	1/36 (2.8%)
Previous MI	20/36 (55.6%)
Clinical presentation	
Stable coronary heart disease	28/36 (77.8%)
Unstable angina	4/36 (11.1%)
NSTEMI	4/36 (11.1%)

Data are presented as mean ± SD, median [quartiles], or n/N (%), as appropriate. BMI, body mass index; CABG, coronary artery bypass surgery; CAD, coronary artery disease; MI, myocardial infarction; NSTEMI, non–ST-elevation myocardial infarction; PCI, percutaneous coronary intervention.

Time requirements for RWS_{Angio} computation and RWS_{OCT} analysis

Using an off-the-shelf workstation with an octa-core Intel i9-10885H processor (Intel Corporation; 2.4 GHz) and 64 GB of random-access memory, the averaged time of RWS_{OCT} analysis for each lesion, counting from OCT pullback loading until the obtainment of RWS_{OCT} results, was 95.0 ± 41.1 minutes. Manual adjustment for frame selection, lumen delineation, lesion selection, and/or inappropriate matching of the cardiac phase was performed in 25 (55.6%) RWS_{Angio} analyses. The average time for RWS_{Angio} analysis for each lesion, counting from the moment when the angiogram was loaded in the software package until the obtainment of RWS_{Angio} results, was 0.9 ± 0.1 minutes.

Reproducibility of RWS_{Angio} analysis

The intraclass correlation coefficients for intra- and interobserver variability in repeated RWS_{Angio} analysis were 0.92 (95% CI, 0.87-0.95) and 0.88 (95% CI, 0.81-0.92), respectively.

Discussion

The main findings of the present study can be summarized as follows: (1) RWS can be rapidly and accurately computed from dynamic angiographic runs, providing a reliable and cost-effective solution for a simplified biomechanical assessment in the catheterization laboratory; and (2) RWS_{Angio} in atherosclerotic segments is significantly higher than in normal segments, showing the potential of RWS_{Angio} to track lipid-rich segments and vulnerable spots along the vessel.

Table 2. Baseline lesion characteristics.

Vessels	N = 38
Interrogated vessel	
Left anterior descending	23/38 (60.5%)
Diagonal	2/38 (5.3%)
Left circumflex	0/38 (0.0%)
Obtuse marginal	2/38 (5.3%)
Ramus intermedius	0/38 (0.0%)
Right coronary artery	11/38 (28.9%)
Lesions	N = 45
Lesion location	
Proximal	20/45 (44.4%)
Middle	19/45 (42.2%)
Distal	6/45 (13.3%)
Minimum lumen area,[a] mm^2	2.67 [2.13, 3.06]
Percent diameter stenosis, %	35 [31, 40]
Lesion length,[a] mm	11.0 [9, 14.2]

Data are presented as median [quartiles] or n/N (%), as appropriate.
[a] Measured by optical coherence tomography.

The prognostic value of coronary strain has been validated by multiple studies.[12,16,18,20,23] A recent study has proven that high-strain spots can accurately identify the vulnerable plaque with high lipid-to-cap ratio and the presence of thin-cap fibroatheroma.[16] In addition to the ability of detecting these vulnerable features, coronary strain is impacted by both cyclic intravascular pressure change and tissue composition inside the vessel wall, thus showing the potential to serve as a more comprehensive index with improved prognostic value.[11–13] Therefore, palpography or elastography were proposed to derive coronary strain from IVUS radiofrequency signals.[12–14,17–20] The rationale relies on the real-time recording of luminal deformation over cardiac cycle. However, as an add-on to IVUS imaging, the in vivo measurement of palpography or elastography tends to be inevitably impacted by the relative displacement between imaging catheter and target tissue, secondary to cardiac motion. By performing FEA on the geometric model reconstructed from coronary images, the above-mentioned limitations of palpography and elastography could be circumvented and extensive biomechanical information, including strain, stress, and luminal deformation over the cardiac cycle, can be obtained with great detail.[21] The geometric models for FEA could be precisely derived from OCT, IVUS, magnetic resonance imaging, or their combination, as long as the detailed plaque composition is clearly visualized and characterized.[21,26–28] The requirement for additional medical resources somehow restricts the clinical application of plaque model-based FEA.

As an essential diagnostic tool for coronary artery disease, angiography directly records the dynamic changes of lumen contour over the cardiac cycle, which corresponds to radial strain, one of the most important components of coronary strain, along with circumferential strain. The direct assessment of radial strain from angiography had never been exploited hitherto because of the prohibitive workload; it required manual quantification of every single frame in the angiographic loop, with a high demand for precision. This limitation has currently been circumvented by AI, which enables fast and accurate performance in cumbersome or repetitive tasks. Thus, the most burdening tasks for the analysis, such as frame selection or frame-by-frame lumen segmentation, can now be automatically completed by the quantification software empowered by AI within 1 minute on average.[29,30] To our knowledge, the present pilot study is the first one to validate RWS_{Angio} versus a normal value obtained from intracoronary imaging standards, in this case OCT and subsequent FEA, and all the analyzable lesions were enrolled in the present study.

The optimal image resolution and physical properties of OCT enable detailed tissue characterization, thus providing the most accurate geometric model for FEA. The position-specific intracoronary pressure derived from pressure tracing data and the virtual pullback curve further ensure the reliable FEA results using OCT. Overall, RWS_{Angio} showed excellent agreement with RWS_{OCT} (Lin coefficient = 0.85), but our study has also unveiled some subtle systematic biases: the slope of 1.21 and the intercept of −2.18 in orthogonal regression might indicate some proportional and constant bias, respectively, of RWS_{Angio} compared with RWS_{OCT}. The systematic differences between OCT and angiography for the quantification of lumen diameter,[31] the projection-dependent calculation of RWS_{Angio} especially for asymmetric lesions, or cardiac motion artefacts[32] (excluded from OCT FEA while RWS_{Angio} comprises all external forces exerted on the plaque) might be factors contributing to explain these systematic differences. Because of the retrospective nature of the present study, the angiographic view for RWS_{Angio} analysis may not always be acquired at the optimal projection. Future prospective studies are warranted to

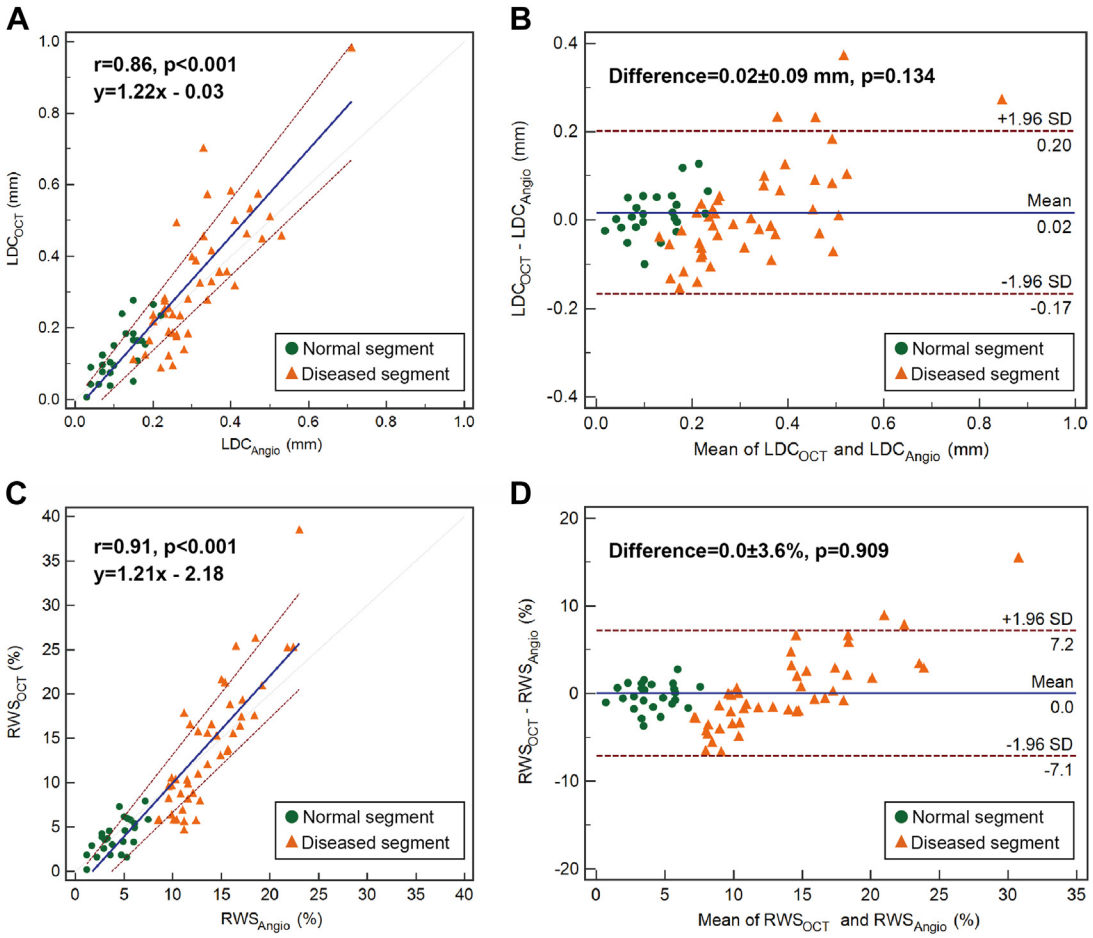

Figure 4.
Passing-Bablok nonparametric regression and Bland-Altman plot for LDC and RWS derived from OCT and angiography. LDC, lumen diameter change; OCT, optical coherence tomography; RWS, radial wall strain.

investigate the performance of RWS_{Angio} when the angiogram is systematically acquired at the optimal projections. Preprocedural planning using multislice coronary computed tomography or angiography-based viewing angle optimization is able to provide us with an accurate and efficient solution for determinizing the optimal projection. In spite of the observed negative correlation between LSR and RWS_{OCT} and RWS_{Angio} difference, most of the asymmetric lesions were biomechanically abnormal, with both high RWS_{Angio} and high RWS_{OCT}. As a result, an agreement of 100% was observed in the present study between RWS_{Angio} and RWS_{OCT} for discriminating normal and abnormal asymmetric lesions, indicating that the suboptimal angiographic projection for asymmetric lesions may not severely impair the diagnostic performance of RWS_{Angio}.

The present study also observed a significantly higher RWS_{OCT} in atherosclerotic segments than in normal segments, which is consistent with previous evidence.[12] Of note, the normal segments in the present study were carefully selected based on coregistered OCT images, considering the frequent occurrence of plaque in angiographically "normal" segments.[33] A recent study also reported a nonnegligible portion (nearly one-third) of the lipid area detected in thin-wall non-culprit coronary artery regions.[34]

Clinical perspectives

Notwithstanding the demonstrated benefits of physiological guidance for revascularization, a significant number of deferred non–flow-limiting lesions may progress or cause acute events.[35–38] Detailed spatial resolution provided by intracoronary imaging enables the accurate identification of plaque vulnerability features, thus ensuring an improved risk stratification.[15] A previous study has found that RWS_{Angio} showed excellent diagnostic performance in identifying OCT-derived

Table 3. LDC and RWS in normal and stenotic segments.

	LDC (mm)			RWS (%)		
	LDC_{Angio} (mm)	LDC_{OCT} (mm)	*P* value	RWS_{Angio} (%)	RWS_{OCT} (%)	*P* value
Normal segments (n = 25)	0.10 [0.07, 0.15]	0.12 [0.08, 0.17]	.088	4.5 [2.9, 5.5]	3.7 [2.4, 5.5]	.510
Stenotic segments (n = 45)	0.29 [0.24, 0.38]	0.29 [0.19, 0.46]	.765	12.6 [11.0, 16.0]	13.1 [8.2, 17.7]	.800
P value	<.001	<.001	–	<.001	<.001	–

Data are presented as median [quartiles].
LDC, lumen diameter change; OCT, optical coherence tomography; RWS, radial wall strain.

vulnerable features such as high lipid-to-cap ratio and the presence of thin-cap fibroatheroma.[16] Compared with the pure morphological assessment, the modest specificity of which has substantially limited its clinical translation for the prediction of future adverse events,[6–9] intracoronary biomechanics are providing a more direct alternative for risk assessment, as plaque rupture is ultimately a mechanical process that can be accurately modeled, simulated, and predicted from the interplay between forces, pressures, and plaque composition within the coronary wall. Indeed, plaque structural stress shows excellent prognostic value for an improved risk stratification.[26] The previous OCT FEA studies have observed a good concordance between strain and plaque structural stress change at the superficial layer of the vessel wall,[21] which invited us to explore the possibility of using angiography-derived wall strain for a simplified assessment method. It should be acknowledged, however, that higher coronary strain does not necessarily lead to higher plaque stress. Historically, wall strain was derived from IVUS as surrogate to detect lipid-rich plaques at times where tissue characterization was not properly developed yet in invasive imaging.[17,19,20] Wall strain soon revealed itself as an independent predictor of events,[12] thus potentially complementing the risk stratification achieved by physiology, morphology,[6,8] or the combination of both in morphofunctional approaches.[15] The major step forward of the methodology hereby proposed in the current study (RWS_{Angio}) is the universal accessibility of every single patient undergoing angiography to a biomechanical assessment. This simplicity, available on a single angiographic projection at an adequate frame rate, enables its application in large-scale studies in a timely fashion by generating the compelling evidence missing so far from the use of more complex and expensive methods to derive RWS.[3,39]

In the near future, by combining RWS_{Angio} with angiography-based physiological assessment, we may be able to achieve improved risk stratification solely from this ubiquitous imaging modality. As to non–flow-limiting stenoses, we can investigate the additional safety of deferring stenting when the stenosis shows low RWS_{Angio}. Conversely, one can test the value of performing targeted intracoronary imaging when a stenosis has a high RWS_{Angio} and adjust medical and interventional treatment accordingly.

Limitations

The present study is limited by its post hoc design and modest sample size and is thus underpowered for specific subgroup analysis or additional exploratory side questions. Bifurcation and stented lesions were excluded from the comparison in this pilot study. In addition, and by chance, no circumflex vessel could be included. The vessels with long, diffuse, and/or heavily calcified lesions were also not included in the present study. The performance of RWS_{Angio} in these disease subsets merits further investigation. In the current study, the angiograms were acquired at an unusually high frame rate (25 frames/s) for coronary applications. Whether this frame rate might be reduced in future studies without jeopardizing the accuracy of RWS_{Angio} calculation will deserve specific clarification. In addition, the exact location of maximal RWS can be slightly different between angiography and OCT but was expected to be of limited clinical relevance.

Notwithstanding the overall good agreement between RWS_{Angio} and RWS_{OCT}, the observation of larger discordance in asymmetric lesions certainly leaves room for further improvement of the methodology.

Although OCT followed by FEA showed consistent results with previous biomechanical and clinical studies[21] and perhaps remains the best currently available method for RWS calculation, the plaque composition used for FEA was derived from OCT using deep learning and the validation studies against histology are still lacking.

Conclusions

With the assistance of AI, RWS_{Angio} can be rapidly and easily computed from coronary angiography alone and shows good agreement with the strain derived from coregistered OCT. This novel and simple method might provide an opportunity for cost-effective and generalizable biomechanical assessment in large populations undergoing angiography.

Declaration of competing interest

Shengxian Tu reports research grants and consultancy from Pulse Medical. William Wijns reports research grants and honoraria from MicroPort, is a medical advisor of Rede Optimus Research, and is cofounder of Argonauts, an innovation facilitator. Jiayue Huang, Huihong Hong, Zhiqing Wang, Lianglong Chen, Juan Luis Gutiérrez-Chico, and Chunming Li reported no financial interests.

Funding sources

Shengxian Tu acknowledges the support of the Natural Science Foundation of China [grant numbers 82020108015 and 81871460]. William Wijns acknowledges the support of a Science Foundation Ireland Research Professorship Award [grant number 15/RP/2765].

Ethics statement and patient consent

The local Ethics Committee of Campo de Gibraltar Health Trust approved the protocol, and each patient gave written informed consent before inclusion.

Supplementary material

To access the supplementary material accompanying this article, visit the online version of the Journal of the Society for Cardiovascular Angiography & Interventions at 10.1016/j.jscai.2022.100570.

References

1. Burke AP, Farb A, Malcom GT, Liang YH, Smialek J, Virmani R. Coronary risk factors and plaque morphology in men with coronary disease who died suddenly. *N Engl J Med*. 1997;336(18):1276–1282.
2. Virmani R, Kolodgie FD, Burke AP, Farb A, Schwartz SM. Lessons from sudden coronary death: a comprehensive morphological classification scheme for atherosclerotic lesions. *Arterioscler Thromb Vasc Biol*. 2000;20(5):1262–1275.
3. Nissen SE. Vulnerable plaque and Einstein's definition of insanity. *J Am Coll Cardiol*. 2020;75(12):1383–1385.
4. Cheruvu PK, Finn AV, Gardner C, et al. Frequency and distribution of thin-cap fibroatheroma and ruptured plaques in human coronary arteries: a pathologic study. *J Am Coll Cardiol*. 2007;50(10):940–949.
5. Virmani R, Burke AP, Farb A, Kolodgie FD. Pathology of the vulnerable plaque. *J Am Coll Cardiol*. 2006;47(8)(suppl):C13–C18.
6. Stone GW, Maehara A, Lansky AJ, et al. A prospective natural-history study of coronary atherosclerosis. *N Engl J Med*. 2011;364(3):226–235.
7. Calvert PA, Obaid DR, O'Sullivan M, et al. Association between IVUS findings and adverse outcomes in patients with coronary artery disease: the VIVA (VH-IVUS in Vulnerable Atherosclerosis) study. *JACC Cardiovasc Imaging*. 2011;4(8):894–901.
8. Prati F, Romagnoli E, Gatto L, et al. Relationship between coronary plaque morphology of the left anterior descending artery and 12 months clinical outcome: the CLIMA study. *Eur Heart J*. 2020;41(3):383–391.
9. Cheng JM, Suoniemi M, Kardys I, et al. Plasma concentrations of molecular lipid species in relation to coronary plaque characteristics and cardiovascular outcome: results of the ATHEROREMO-IVUS study. *Atherosclerosis*. 2015;243(2):560–566.
10. Wu X, von Birgelen C, Zhang S, Ding D, Huang J, Tu S. Simultaneous evaluation of plaque stability and ischemic potential of coronary lesions in a fluid-structure interaction analysis. *Int J Cardiovasc Imaging*. 2019;35(9):1563–1572.

11. Serruys PW, García-García HM, Buszman P, et al. Effects of the direct lipoprotein-associated phospholipase A(2) inhibitor darapladib on human coronary atherosclerotic plaque. *Circulation*. 2008;118(11):1172–1182.
12. Schaar JA, Regar E, Mastik F, et al. Incidence of high-strain patterns in human coronary arteries: assessment with three-dimensional intravascular palpography and correlation with clinical presentation. *Circulation*. 2004;109(22):2716–2719.
13. Van Mieghem CA, McFadden EP, de Feyter PJ, et al. Noninvasive detection of subclinical coronary atherosclerosis coupled with assessment of changes in plaque characteristics using novel invasive imaging modalities: the Integrated Biomarker and Imaging Study (IBIS). *J Am Coll Cardiol*. 2006;47(6):1134–1142.
14. Li Z, Wang L, Hu X, et al. Effect of rosuvastatin on atherosclerotic plaque stability: an intravascular ultrasound elastography study. *Atherosclerosis*. 2016;248:27–35.
15. Hong H, Jia H, Zeng M, et al. Risk stratification in acute coronary syndrome by comprehensive morphofunctional assessment with optical coherence tomography. *JACC Asia*. 2022;2(4):460–472.
16. Hong H, Li C, Gutiérrez-Chico JL, et al. Radial wall strain: a novel angiographic measure of plaque composition and vulnerability. *EuroIntervention*. Published online September 8, 2022. https://doi.org/10.4244/EIJ-D-22-00537
17. de Korte CL, van der Steen AF. Intravascular ultrasound elastography: an overview. *Ultrasonics*. 2002;40(1-8):859–865.
18. de Korte CL, Pasterkamp G, van der Steen AF, Woutman HA, Bom N. Characterization of plaque components with intravascular ultrasound elastography in human femoral and coronary arteries in vitro. *Circulation*. 2000;102(6):617–623.
19. de Korte CL, Sierevogel MJ, Mastik F, et al. Identification of atherosclerotic plaque components with intravascular ultrasound elastography in vivo: a Yucatan pig study. *Circulation*. 2002;105(14):1627–1630.
20. de Korte CL, Carlier SG, Mastik F, et al. Morphological and mechanical information of coronary arteries obtained with intravascular elastography; feasibility study in vivo. *Eur Heart J*. 2002;23(5):405–413.
21. Huang J, Yang F, Gutiérrez-Chico JL, et al. Optical coherence tomography-derived changes in plaque structural stress over the cardiac cycle: a new method for plaque biomechanical assessment. *Front Cardiovasc Med*. 2021;8:715995.
22. Wu X, von Birgelen C, Li Z, et al. Assessment of superficial coronary vessel wall deformation and stress: validation of in silico models and human coronary arteries in vivo. *Int J Cardiovasc Imaging*. 2018;34(6):849–861.
23. Kwak BR, Bäck M, Bochaton-Piallat ML, et al. Biomechanical factors in atherosclerosis: mechanisms and clinical implications. *Eur Heart J*. 2014;35(43):3013–3020.
24. Suwannasom P, Sotomi Y, Asano T, et al. Change in lumen eccentricity and asymmetry after treatment with Absorb bioresorbable vascular scaffolds in the ABSORB cohort B trial: a five-year serial optical coherence tomography imaging study. *EuroIntervention*. 2017;12(18):e2244–e2252.
25. Chu M, Jia H, Gutiérrez-Chico JL, et al. Artificial intelligence and optical coherence tomography for the automatic characterisation of human atherosclerotic plaques. *EuroIntervention*. 2021;17(1):41–50.
26. Costopoulos C, Maehara A, Huang Y, et al. Heterogeneity of plaque structural stress is increased in plaques leading to MACE: insights from the PROSPECT study. *JACC Cardiovasc Imaging*. 2020;13(5):1206–1218.
27. Wang L, Tang D, Maehara A, et al. Fluid-structure interaction models based on patient-specific IVUS at baseline and follow-up for prediction of coronary plaque progression by morphological and biomechanical factors: a preliminary study. *J Biomech*. 2018;68:43–50.
28. Guo X, Zhu J, Maehara A, et al. Quantify patient-specific coronary material property and its impact on stress/strain calculations using in vivo IVUS data and 3D FSI models: a pilot study. *Biomech Model Mechanobiol*. 2017;16(1):333–344.
29. Zhao Q, Li C, Chu M, Gutiérrez-Chico JL, Tu S. Angiography-based coronary flow reserve: the feasibility of automatic computation by artificial intelligence. *Cardiol J*. Published online August 6, 2021. https://doi.org/10.5603/CJ.a2021.0087
30. Gutiérrez-Chico JL, Liu L, Chu M, et al. The role of superficial wall stress and mechanical factors in scaffold failure: protocol of the RANSOMED study. *Cardiol J*. 2022;29(2):319–323.
31. Gutiérrez-Chico JL, Serruys PW, Girasis C, et al. Quantitative multi-modality imaging analysis of a fully bioresorbable stent: a head-to-head comparison between QCA, IVUS and OCT. *Int J Cardiovasc Imaging*. 2012;28(3):467–478.
32. Chu M, Cortés C, Liu L, et al. Comprehensive appraisal of cardiac motion artefact in optical coherence tomography. Cardiol J. Published online October 28, 2021. https://doi.org/10.5603/CJ.a2021.0137
33. Mintz GS, Painter JA, Pichard AD, et al. Atherosclerosis in angiographically "normal" coronary artery reference segments: an intravascular ultrasound study with clinical correlations. *J Am Coll Cardiol*. 1995;25(7):1479–1485.
34. Tomaniak M, Hartman EMJ, Tovar Forero MN, et al. Near-infrared spectroscopy to predict plaque progression in plaque-free artery regions. *EuroIntervention*. 2022;18(3):253–261.
35. Chan KH, Chawantanpipat C, Gattorna T, et al. The relationship between coronary stenosis severity and compression type coronary artery movement in acute myocardial infarction. *Am Heart J*. 2010;159(4):584–592.
36. Glaser R, Selzer F, Faxon DP, et al. Clinical progression of incidental, asymptomatic lesions discovered during culprit vessel coronary intervention. *Circulation*. 2005;111(2):143–149.
37. Sanidas EA, Mintz GS, Maehara A, et al. Adverse cardiovascular events arising from atherosclerotic lesions with and without angiographic disease progression. *JACC Cardiovasc Imaging*. 2012;5(3):S95–S105. suppl.
38. Narula J, Nakano M, Virmani R, et al. Histopathologic characteristics of atherosclerotic coronary disease and implications of the findings for the invasive and noninvasive detection of vulnerable plaques. *J Am Coll Cardiol*. 2013;61(10):1041–1051.
39. Arbab-Zadeh A, Fuster V. From detecting the vulnerable plaque to managing the vulnerable patient: JACC state-of-the-art review. *J Am Coll Cardiol*. 2019;74(12):1582–1593.